Received: 23 May 2023 | Revised: 17 November 2023 | Accepted: 26 November 2023

DOI: 10.1002/ar.25368

RESEARCH ARTICLE

The Anatomical Record WILEY

Comparing age- and bone-related differences in collagen fiber orientation: A case study of bats and laboratory mice using quantitative polarized light microscopy

Tobin Lee Hieronymus[1,2] | **David A. Waugh**[1,2] | **Hope C. Ball**[1,2] | **Christopher J. Vinyard**[3] | **Alex Galazyuk**[1] | **Lisa Noelle Cooper**[1,2]

[1]Department of Anatomy and Neurobiology, Northeast Ohio Medical University, Rootstown, Ohio, USA

[2]Musculoskeletal Research Focus Area, Northeast Ohio Medical University, Rootstown, Ohio, USA

[3]Department of Biomedical Sciences, Ohio University, Athens, Ohio, USA

Correspondence
Tobin Lee Hieronymus, Department of Anatomy and Neurobiology, Northeast Ohio Medical University, Rootstown, OH, USA.
Email: thieronymus@neomed.edu

Funding information
National Science Foundation, Grant/Award Number: 1537745

Abstract

As bones age in most mammals, they typically become more fragile. This state of bone fragility is often associated with more homogenous collagen fiber orientations (CFO). Unlike most mammals, bats maintain mechanically competent bone throughout their lifespans, but little is known of positional and age-related changes in CFO within wing bones. This study tests the hypothesis that age-related changes in CFO in big brown bats (*Eptesicus fuscus*) differ from those of the standard mammalian model for skeletal aging, the C57BL/6 laboratory mouse. We used data from quantitative polarized light microscopy (qPLM) to compare CFO across the lifespan of long-lived big brown bats and age matched C57BL/6 mice. *Eptesicus* and C57BL/6 mice displayed idiosyncratic patterns of CFO. Consistent age-related changes were only apparent in the outer cortical bone of *Eptesicus*, where bone tissue is more longitudinally arranged and more anisotropic in older individuals. Both taxa displayed a ring of more transversely oriented bone tissue surrounding the medullary cavity. In *Eptesicus*, this tissue represents a greater proportion of the overall cross-section, and is more clearly helically aligned (arranged at 45° to the bone long axis) than similar bone tissue in mice. Bat wing bones displayed a proximodistal gradient in CFO anisotropy and longitudinal orientation in both outer and inner cortical bone compartments. This study lays a methodological foundation for the quantitative evaluation of bone tissue architecture in volant and non-volant mammals that may be expanded in the future.

KEYWORDS

aging, bat, bone, collagen fiber orientation, mouse, polarized light microscopy

Abbreviations: ACG, angular central Gaussian distribution; CFO, collagen fiber orientation; CPL, circularly polarized light microscopy; qPLM, quantitative polarized light microscopy; RDA, redundancy analysis; ROI, region of interest; VARPART, variation partitioning analysis.

1 | INTRODUCTION

1.1 | Wing bone performance and phenotype in bats

Bats are the only mammals to have achieved powered flight (Cooper et al., 2012; Cooper & Sears, 2013), and accordingly evolved unique skeletal phenotypes and performance. The wing bones of bats function in controlled deformation, rather than stiffness (Swartz & Middleton, 2008). Unlike terrestrial taxa, the humerus and radius of bats undergo significant torsional loading during wingbeats (Swartz et al., 1992). The metacarpals and phalanges form most of the surface of the wing and undergo large bending deformations such that they alternate between dorsal and ventrally concave shapes and the chord lengths (straight end-to-end lengths) of these elements reduce to ~60% of the arc lengths (length along the curvature of the diaphysis) (Swartz et al., 2007; Swartz & Middleton, 2008). Wing bones experience strain reversal with each wingbeat, oscillating between compression and tension (Swartz & Middleton, 2008). These bending loads are thought to contribute to the spatial and temporal distribution of vortices in flight (Lucas et al., 2014). How the bones of bats undergo substantial deformations and remain resilient to fracture is poorly understood. We do not know the full suite of compositional innovations creating their unusual performance abilities, nor do we understand how these traits change with age.

Compared to other mammals, the forelimb bones of bats are long (Sears et al., 2006), display thin, circular cortices, and are typically poorly vascularized such that bones of large-bodied bats display few vascular canals (Andronowski et al., 2022; Foote, 1916; Lee & Simons, 2015; Pratt et al., 2018; Skedros & Doutré, 2019). In addition, density of wing bones decreases from bone-to-bone along a proximodistal gradient, accompanied by a parallel reduction in stiffness (Bennett & Forwood, 2010; Papadimitriou et al., 1996; Swartz et al., 2007; Swartz & Middleton, 2008). These characteristics contribute to the specialized performance of wing bones during flight.

Bone, in general, is a dynamic organ that is mechanosensitive and preferentially orients collagens within its extracellular matrix to align in a manner that correlates with principal strains, as shown in studies of horses (Boyde & Riggs, 1990; Skedros et al., 2009), macaques (Bromage, 1992), sheep, and deer (Skedros et al., 2009). Despite the prevalence of torsional loading in bats, histological studies show these bones share broadly similar collagen fiber orientations with other mammals (Skedros & Doutré, 2019).

With advanced age, mammalian bone typically declines in mechanosensitivity, mineral density, and integrity of collagens, and CFO becomes more homogenous (Goldman et al., 2003). This deterioration in bone results in fragility. Bats live 3–10 times longer than similarly-sized land mammals (Doherty & de Magalhaes, 2016; Munshi-South & Wilkinson, 2010; Podlutsky et al., 2005; Wilkinson & Adams, 2019; Wilkinson & South, 2002), have extended healthspans (Huang et al., 2019; Seluanov et al., 2018), and are considered ideal models for aging studies (Austad, 2010; Austad & Fischer, 1991; Ball et al., 2018; Brunet-Rossinni & Austad, 2004; de Medina, 2019; Gomes et al., 2011; Lidzbarsky et al., 2018; Ma & Gladyshev, 2017; Pride et al., 2015; Salmon et al., 2009; Wilkinson et al., 2021). The aim of this study was to compare strategies of skeletal aging in long-lived big brown (*Eptesicus fuscus*) and comparatively short-lived C57BL/6 mice based on quantitative measures of collagen fiber orientation in bone.

1.2 | Study system

We examined age-related changes in CFO in big brown bats (*Eptesicus*) and the C57BL/6 mouse strain. Bats as a group have been the subject of intense skeletobiology research into the development and patterning of the wing and its supporting bones (Andronowski et al., 2022; Cooper et al., 2012; Cooper et al., 2018; Cooper & Sears, 2013; Hockman et al., 2008; Sears et al., 2006; Weatherbee et al., 2006) and wing bone performance (Swartz et al., 1992; Swartz et al., 2007), but little is known of their skeletal response to aging. *Eptesicus* have a lifespan of approximately 20 years (Wilkinson et al., 2021; Wilkinson & South, 2002). In contrast, C57BL/6 mice are one of the most common strains for biomedical studies of the aging skeleton, and their age-related phenotypes are well documented (Beamer et al., 1996; Brodt et al., 1999; Dengler-Crish et al., 2016; Dengler-Crish et al., 2018; Ferguson et al., 2003; Halloran et al., 2002; Holguin et al., 2014; Jilka, 2013; Sheng et al., 1999). C57BL/6 mice are also relatively long-lived for laboratory mice—their median lifespan is 866 days for females and 901 days for males (Yuan et al., 2009).

Although phenotypes of bones have been compared between bats and terrestrial mammals, no studies have undertaken quantitative comparisons of collagen fiber orientation across lifespan. This study utilizes quantitative polarized light microscopy to identify morphological subregions within the cortices of long bones, describe how these subregions differ between a volant bat (*Eptesicus*) and a standard laboratory mouse (C57BL/6), and track age-related changes in these subregions.

1.2.1 | Hypothesis

We expect that collagen orientation within the long bone cortices of *Eptesicus* will display a unique morphology that differs significantly with that of C57BL/6 mice, and that the trajectory of age-related changes in collagen orientation will also differ between the two taxa.

2 | METHODS

2.1 | Quantitative polarized light microscopy

This study employs polarized light microscopy, which has become a standard tool for investigating collagen fiber orientation in histological sections. Optical systems for polarized light microscopy can be grouped into three general configurations: crossed linear polarizers (Boyde et al., 1984); crossed circular polarizers (circularly polarized light microscopy or CPL (Boyde et al., 1984; Bromage et al., 2003; Warshaw et al., 2017); and a combination of circular polarizer and rotating linear analyzer, where the rotation of the optical axis of the analyzer is mechanical (Glazer et al., 1996) or electro-optical (Oldenbourg & Mei, 1995), often referred to as quantitative polarized light microscopy (qPLM, Kaminsky et al., 2007; Sekita et al., 2017; Spiesz et al., 2011; Spiesz et al., 2013; Spiesz et al., 2018) or 3D polarized light microscopy (3dPLM, Yang et al., 2018). CPL has become the most commonly used approach, because it is easy to implement on most microscope systems and provides a direct readout of out-of-plane CFO (deviation from microscope optical axis, *theta* [θ], Figure 1) that is not affected by in-plane CFO (azimuth, *phi* [φ]). In CPL, collections of fibers that are isotropic or anisotropic with a predominantly longitudinal orientation appear dark, whereas anisotropic fibers that are transverse-to-obliquely oriented are bright (Bromage et al., 2003) (Figure 1). In diaphyseal cross-section, longitudinally-oriented fibers are associated with high tensile strain resistance, transversely-oriented fibers are thought to better resist compressive strains (Goldman et al., 2003), and obliquely- or helically-oriented collagens are expected to optimize resistance to strain in torsion or shear (De Margerie et al., 2005; Skedros & Doutré, 2019).

For this study, we employ qPLM, which provides additional details on CFO when compared to CPL. Although many implementations of this configuration

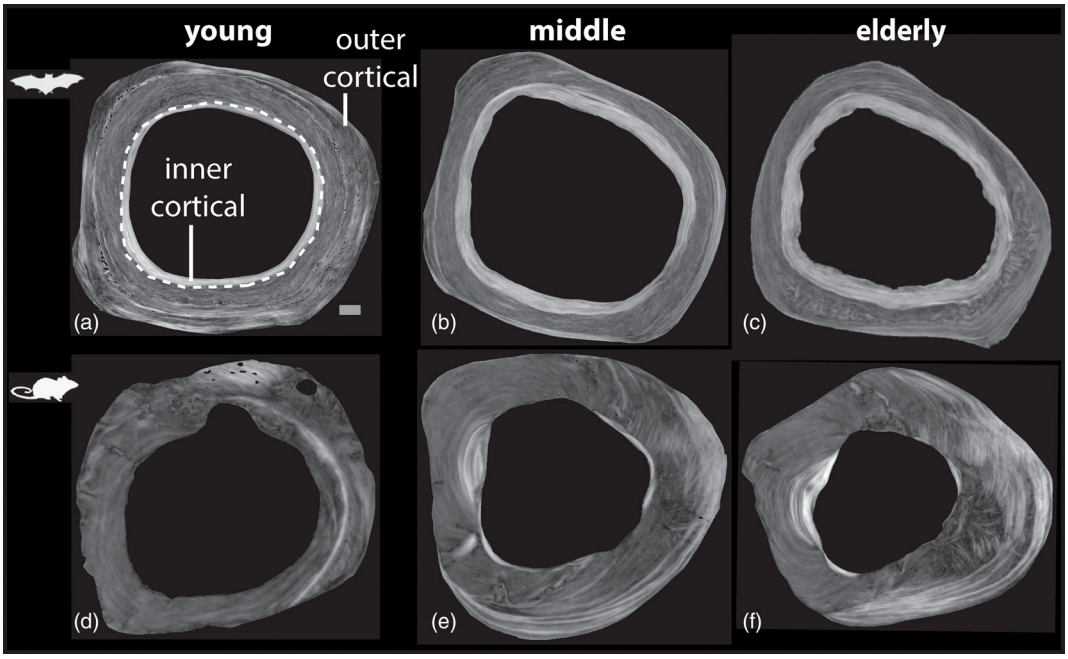

FIGURE 1 qPLM images of unstained ground sections through the midshaft of the radius of long-lived big brown bat (*Eptesicus fuscus*, a–c) and C57BL/6 laboratory mice (d–f) from young (left), middle-aged (middle), and elderly (right) age groups. The collagen fiber orientations shown in these qPLM images are similar to CPL images, where longitudinally oriented fibers are dark, compared to more transversely- or obliquely-oriented fibers (light-colored). A distinct inner tissue compartment lies adjacent to the medullary cavity in the center of the bone cross-section. In most sections, collagens within the inner cortical region display a different pattern of orientation compared to those in outer cortical bone. Inner and outer cortical regions are separated by a dashed line in (a). All images are the same size, and not to scale, to illustrate the different relative sizes of the inner cortical and periosteal compartments.

are technically advanced and require dedicated microscopes, in principle there are only two components that separate qPLM configurations from CPL: repeatable manipulation of an elliptical or linear polarizing element, and a small amount of image post-processing. With little additional hardware and modest processing, qPLM configurations provide a readout of both out-of-plane and in-plane collagen fiber orientation (Figure 2). The out-of-plane orientation θ from qPLM is directly comparable to calibrated grayscale value in CPL. The additional in-plane CFO measure φ is directly comparable to estimation of fast axis with a full wave plate and crossed linear polarizers. Because of the distributions of these two measurements are linked, and because standard parametric statistics on orientation data can provide misleading results, we apply directional statistics (Mardia & Jupp, 2000; Tyler, 1987) as an approach to describing CFO. We have bundled the image processing for qPLM together with directional statistical analyses in a package for the R statistical computing environment (R Core Team, 2018), so that this approach can be freely modified and expanded.

2.1.1 | Animals

This study used known-aged colonies of big brown bats (*Eptesicus fuscus*) and C57BL/6 mice (Jackson Laboratories) maintained by the Cooper lab at NEOMED (Rootstown, Ohio, USA; Table 1). All *Eptesicus* are kept in a large non-breeding colony for at least 1 year at a constant temperature, and the bats do not undergo annual torpor or hibernation. *Eptesicus* have an adult body mass around 20 g, and mass of C57BL/6 mice is slightly larger with masses that range from 25 to 36 g. From our known-aged colonies, *Eptesicus* and age-matched C57BL/6 mice were assigned into young, middle, and elderly age categories (Table 1) based on published evidence of lifespan in mice (Flurkey et al., 2007) and the longevity of bats (Wilkinson & South, 2002). Age categories for the bats included young (1–4 years), middle (5–9 years), and elderly (10+ years). Normalized age-matched categories for the mice included young (4 weeks-3 months), middle (6–16 months), and elderly (18+ months) (Flurkey et al., 2007; Yuan et al., 2009). Our samples, taken from young, middle, and elderly

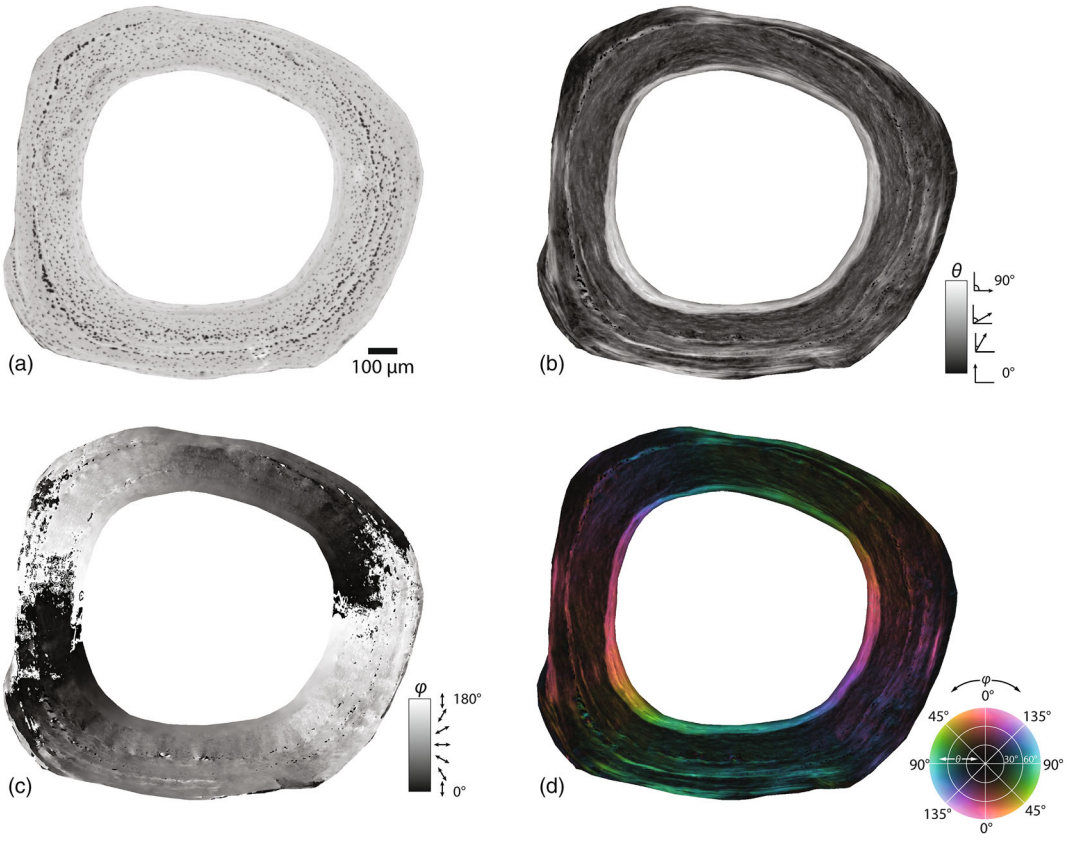

FIGURE 2 Quantitative Polarized Light Microscopy (qPLM) overview, shown with a section from a radius of Eptesicus fuscus. Rotating-polarizer qPLM analysis software [Rotopol™ (Kaminsky et al., 2007)] returns three variables for each pixel, describing (a) the transmissivity I, (b) the retardance $|\sin \delta|$, shown here converted to out-of-plane orientation θ, and (c) the in-plane orientation φ. The combination of θ and φ is shown in (d) using a perceptually scaled combination of brightness (mapped to θ) and hue (mapped to φ).

TABLE 1 Bone samples used for density (a) and histology (b) assays.

(a)	Bone density				
	Taxon	**Bone**	**Young**	**Middle**	**Elderly**
	Eptesicus	Humerus	9 (3M, 3/3F)	3 (0M, 0/3F)	8 (2M, 4/2F)
	Eptesicus	Radius	9 (3M, 3/3F)	4 (0M, 1/3F)	8 (2M, 4/2F)
	Eptesicus	Metacarpal	9 (3M, 3/3F)	4 (0M, 1/3F)	8 (2M, 4/2F)
	C57BL/6	Humerus	9 (6M, 3F)	28 (14M, 14F)	15 (5M, 10F)
	C57BL/6	Radius	9 (6M, 3F)	28 (14M, 14F)	15 (5M, 10F)
	C57BL/6	Metacarpal	8 (5M, 3F)	26 (13M, 13F)	15 (5M, 10F)
(b)	**Bone histology**				
	Taxon	**Bone**	**Young**	**Middle**	**Elderly**
	Eptesicus	Humerus	5 (1M, 2/2F)	3 (0M, 0/3F)	3 (1M, 1/1F)
	Eptesicus	Radius	9 (4M, 2/3F)	3 (0M, 0/3F)	5 (2M, 1/2F)
	Eptesicus	Metacarpal	7 (3M, 1/3F)	3 (0M, 0/3F)	5 (2M, 1/2F)
	C57BL/6	Humerus	6 (3M, 3F)	10 (5M, 5F)	5 (2M, 3F)
	C57BL/6	Radius	4 (1M, 3F)	9 (4M, 5F)	5 (2M, 3F)

Note: M indicates males, F indicates females. For female *Eptesicus*, number indicates #colony/#wild individuals.

adults, will therefore reflect age-related shifts in bone phenotype throughout at least 75% of their respective lifespans. This bat colony (Skrinyer et al., 2017) has been used for molecular skeletal biology (Ball et al., 2016) and aging studies (Ball et al., 2018; Wilkinson et al., 2020).

Additional bat samples were obtained from a colony of wild-caught *Eptesicus* maintained by Drs. Jeff Wenstrup and Alex Galazyuk, also at NEOMED. Wild-caught bats within the Wenstrup/Galazyuk colony were categorized into young, middle-aged and elderly age classes based on relative tooth wear (Brunet-Rossinni & Austad, 2004). Mostly unworn teeth with sharp cusps within the pre-molars and molars were classified within the "young" age-class. Conversely, bats with flattened teeth that lacked cusps and crests within their cheek teeth were classified as "elderly." "Middle-aged" bats were therefore distinguished based on moderate wear to the cusps and crests of the cheek teeth. Within the sample of *Eptesicus*, half of the elements included in the analysis are from known age individuals, half are from wild-caught individuals where age is estimated by tooth wear (Table 1). All wild-caught bats were captive for at least a year before sampling for this study. Bats are in a captive colony not exposed to external air or fluctuations in temperature.

C57BL/6 mice are used as a model for osteoporosis research (Ferguson et al., 2003; Jilka, 2013), a disease associated with age-related bone fragility. As such, they have undergone intensive study of age-related deterioration in bone phenotype (Dengler-Crish et al., 2016; Halloran et al., 2002; Raghavan et al., 2012), biomechanics (Aido et al., 2015; Ferguson et al., 2003; Srinivasan et al., 2003), and bone cell signaling (Syed et al., 2010). As C57BL/6 mice age, their long bones erode along the inner cortical surface. Infilling inner cortical bone has a low growth rate (Sheng et al., 1999) but the periosteal perimeter is maintained or new material is added, resulting in a thinner bone with a greater relative cross-sectional moment of inertia (Ferguson et al., 2003). This pattern of inner cortical thinning is also seen in osteoporotic humans and therefore this strain of mouse is considered a model for studying age-related osteopenia and osteoporosis (Ferguson et al., 2003).

2.1.2 | Bone mineral density

Mineral density affects the optical properties of bone under polarized light. To control for this known source of variation, we used bone mineral density data collected for a larger sample of *Eptesicus* and C57BL/6 mice that broadly overlaps with the specimens included in histological analysis. Specifics of the expected contributions of mineral density to the optical properties of bone thin sections are considered in the description of our quantitative polarized light microscopy protocol.

The humerus, radius, and metacarpals (Table 1a) were harvested from cadaveric forelimbs, cleaned and stored in phosphate buffered saline until they underwent high-resolution micro-CT scans in a VivaCT 75 scanner

TABLE 2 Mean bone density values (a) and percentage of inner cortical bone relative to total bone cross-sectional area (b).

(a)	Bone density (g hydroxyapatite/cm^3)				
	Taxon	Bone	Young Mean (SEM)	Middle Mean (SEM)	Elderly Mean (SEM)
	Eptesicus	Humerus	1309.68 (4.08)	1267.93 (11.44)	1243.46 (3.86)
	Eptesicus	Radius	1286.64 (6.13)	1167.15 (5.54)	1158.45 (10.91)
	Eptesicus	Metacarpal	1076.98 (5.62)	1020.48 (4.55)	1019.69 (2.77)
	C57BL/6	Humerus	1094.19 (39.79)	1140.83 (5.47)	1061.69 (4.96)
	C57BL/6	Radius	1013.35 (37.13)	1052.77 (4.94)	1033.02 (2.42)
	C57BL/6	Metacarpal	895.38 (42.70)	1031.83 (2.82)	1001.05 (4.28)
(b)	Percentage inner cortical bone				
	Taxon	Bone	Young Mean (SEM)	Middle Mean (SEM)	Elderly Mean (SEM)
	Eptesicus	Humerus	22.199 (4.614)	14.802 (5.127)	9.652 (2.605)
	Eptesicus	Radius	15.545 (1.335)	14.359 (2.991)	20.044 (4.135)
	Eptesicus	Metacarpal	18.463 (2.478)	11.746 (4.138)	14.701 (1.886)
	C57BL/6	Humerus	0.113	3.564 (0.499)	1.009 (0.133)
	C57BL/6	Radius	0.876	3.238 (0.203)	1.767 (0.197)

Note: Density was measured using stock calibration tools and algorithms for the Scanco VivaCT 75 microCT scanner. Percentage inner cortical bone was based on spatially constrained clustering of collagen fiber orientation distributions about a bone cross-section.

(Scanco Medical AG, Brüttisellen, Switzerland). Voxel grayscale values were calibrated to units of bone mineral density (as mg hydroxyapatite per cm^3) using a Scanco QC phantom and Scanco's built-in algorithm. Mean bone mineral densities for midshaft transverse sections of each scanned element were calculated in ImageJ. Overall mean bone mineral densities by age class and element (Table 2a) were used to scale expected birefringence values for qPLM, ultimately scaling our reported values of out-of-plane orientation.

2.1.3 | Imaging and analysis of the bone extracellular matrix

Humeri and radii of bats and mice, along with third metacarpals of bats (Table 1b), were air-dried, embedded in Buehler Epothin™ epoxy resin and cured at room temperature. Mouse third metacarpal specimens could not be reliably sectioned and were excluded from histological analysis. Because of this omission, we could only fully evaluate proximodistal gradients in CFO distribution in bats. Embedded samples were cut approximately 1 mm to the side of the mid-diaphyseal transverse plane on a Buehler Isomet 1000 low-speed wafering saw with a water-cooled diamond grit blade. Using successively finer grits on a water-cooled lap wheel, the surface was ground and polished to reach the mid-diaphyseal plane before a final polish with P4000 grit. The polished surfaces were then glued to the frosted surface of glass slides with a UV curing resin (Henkel Loctite 349). Excess material was cut off the slide using a water-cooled diamond saw blade before grinding and polishing to a final thickness of approximately 45 μm, with a final polish using P4000 grit. Coverslips were attached to the slides using immersion oil. Final slide thickness was measured optically at four points relative to the imaging orientation around the periosteal surface (approximately dorsal, ventral, medial, and lateral edges of the bones) using a 40× objective lens and a calibrated vernier micrometer microscope stage.

2.1.4 | Quantitative polarized light microscopy

Finished slides were analyzed using a Nikon Eclipse 50i POL polarizing microscope (Nikon, Melville, NY, USA) outfitted with a 532 nm peak, 55 nm full width half maximum (FWHM) bandpass filter (BN532-46, Midwest Optical, Palatine, IL, USA), a Rotopol™ rotating analyzer system (Kaminsky et al., 2007; http://cad4.cpac.washington.edu/ROTOPOLhome/ROTOPOL.htm), and an MA300 digital microscope camera (Amscope, Irvine, CA, USA). Each bone section was captured in a single image frame that contained the entire diaphyseal cross

TABLE 3 Redundancy analysis (RDA) ANOVA results for *Eptesicus* & C57BL/6 inner cortical bone.

	Df	Variance	*F*#	*p*	Holm *p*
Age	1	0.20	2.01	0.087	0.347
Taxon	1	0.68	6.88	0.001*	0.056
Sex	1	0.06	0.55	0.652	0.720
Bone (humerus vs. radius)	1	0.11	1.07	0.360	0.720
Residual	50	2.53			
Age|(Sex, Taxon, Bone)	1	0.12	2.50	0.087	0.347

Note: Full model terms are given first. The last row shows the test of the age class term after accounting for confounding variables. After accounting for multiple testing, none of the terms explain a significant proportion of variation in collagen fiber orientation when inner cortical bone CFO of *Eptesicus* and C57BL/6 are considered together.

*$p < 0.05$.

TABLE 4 Redundancy analysis (RDA) ANOVA results for inner cortical bone within *Eptesicus* only.

	Df	Variance	*F*#	*p*	Holm *p*
Age	1	0.11	1.81	0.167	0.505
Sex	1	0.01	0.12	0.878	0.878
Proximodistal gradient	1	0.39	6.32	0.004*	**0.026***
Residual	40	2.49			
PD gradient|(Age, Sex)	1	0.39	6.32	0.005*	**0.027***
Age|(PD gradient, Sex)	1	0.10	1.60	0.168	0.505

Note: Full model terms are given first. The last two rows show tests of proximodistal gradient and age class terms after accounting for other variables. Proximodistal gradient emerges as a significant explanation of CFO in *Eptesicus* in the full model, and remains significant when other terms are accounted for in the conditional model.

*$p < 0.05$.

section. Rotopol™ control and image capture software returns a set of three false-color RGB images that use the red channel to encode data. These images include optical transmissivity (I, non-birefringent variation in brightness, equivalent to grayscale image with just the band-pass filter; Figure 2a), retardance ($|\sin \delta|$, equivalent to brightness in circular polarized light imaging), and slow axis orientation (φ, analogous to the variation in interference colors visible with a first-order wave plate in linear polarized light imaging; Figure 2c). In addition to serving as the primary data source for analysis, Rotopol™ images were also used to generate binary image masks in Adobe Photoshop to restrict analyses to pixels containing bone tissue.

Processing and analysis of quantitative polarized light microscopy (qPLM) data from the Rotopol™ system was conducted in the R statistical computing environment (R Core Team, 2018) using a collection of functions bundled into an R package we call *microTransit* (available at https://github.com/TobinH/microTransit/releases/tag/v1.0.0). In addition to specific functions for handling Rotopol™ format images, *microTransit* also includes functions that will analyze sets of rotating-polarizer images using the generalized approach of Glazer et al. (Glazer et al., 1996), allowing this package to be flexibly applied to images from any rotating-polarizer configuration, up to and including manual rotation of the linear polarizer/analyzer on a standard polarizing scope.

Thickness measurements at four points across each ground section (intended to capture maximum and minimum image coordinates in u and v, not strictly oriented to anatomical landmarks) were used to fit a linear estimate of specimen thickness at each pixel, to ameliorate the effect of uneven grinding and polishing. Pixel-scale measurements of $|\sin \delta|$ from Rotopol™ analysis software were then transformed into estimates of out-of-plane orientation θ (Figure 2b) using the following relationship:

$$\theta = \sin^{-1}\sqrt{\frac{\left(\sin^{-1}|\sin\delta|\right)\cdot\lambda}{h\cdot n_s}}$$

where λ is the center wavelength of the bandpass filter, h is the estimated thickness of the specimen at that pixel, and n_s is the estimated birefringence of bone tissue in the sample (Nesse, 2004). This operation is built into the *KaminskyqPLM()* and *buildqPLM()* functions in *microTransit*.

	Df	Variance	F#	p	Holm p
Age	1	0.01	0.16	0.777	>1
Taxon	1	0.29	9.97	0.002*	**0.008***
Sex	1	0.01	0.19	0.734	>1
Bone (humerus vs. radius)	1	0.88	30.3	0.001*	**0.001***
Residual	63	1.82			
Age|(Sex, Taxon, Bone)	1	0.004	0.13	0.815	>1

TABLE 5 Redundancy analysis (RDA) ANOVA results for *Eptesicus* & C57BL/6 outer cortical bone.

Note: Full model terms are given first. The last row shows the test of the age class term after accounting for confounding variables. Taxon and skeletal element emerge as terms that explain significant proportions of variation in outer cortical bone CFO across both *Eptesicus* and C57BL/6 mice, but there is no significant age-related signal.
*$p < 0.05$.

	Df	Variance	F#	p	Holm p
Age	1	0.22	7.58	0.009*	**0.034***
Sex	1	0.01	0.32	0.592	0.592
Proximodistal gradient	1	1.63	56.9	0.001*	**0.001***
Residual	40	1.15			
PD gradient|(Age, Sex)	1	1.63	56.9	1e−04*	**0.001***
Age|(PD gradient, Sex)	1	0.19	6.60	0.015*	**0.034***

TABLE 6 Redundancy analysis (RDA) ANOVA results for *Eptesicus* outer cortical bone.

Note: Full model terms are given first. The last two rows show tests of proximodistal gradient and age class terms after accounting for other variables. Both proximodistal gradient and age class are identified as significant terms in the full model, and both remain significant when other variables are accounted for, showing that these are independent effects and not covariance related to sampling.
*$p < 0.05$.

Because specimen birefringence has a direct impact on the estimate of θ, and birefringence is known to change with differences in bone mineral density (Ascenzi & Bonucci, 1961; Bonucci, 2007; Dallemagne & Melon, 1946), we chose to estimate birefringence separately for different bones and age classes in our sample. We used MicroCT measurements of bone density to estimate birefringence using a volumetric model which assumes that bone crystallites and collagen fibers are aligned with each other (i.e., the fast axis of collagen is aligned with the slow axis of hydroxyapatite) and any volume not occupied by hydroxyapatite is filled with collagen. While there is evidence that bone mineral crystallites are not entirely aligned to bone collagen (Skedros et al., 2006; Takano et al., 1996), there is at least some concordance between their orientation in mature osteonal tissue (Ascenzi et al., 1979). Because birefringences are differences between fast and slow axis refractive indices (Nesse, 2004), and the refractive index of a heterogeneous material is simply a weighted sum of the component refractive indices (Stokes, 1963), the simplifying assumption of optical axis alignment between collagen and bone mineral allows us to model the overall birefringence as a sum of bone mineral and collagen birefringence weighted by their proportional volume:

$$n_s = \frac{D_s}{D_{HA}} \cdot n_{HA} + \left(1 - \frac{D_s}{D_{HA}}\right) \cdot n_c$$

where n_{HA} is the reference intrinsic birefringence of hydroxyapatite (-4×10^{-3}), n_c is an estimated form birefringence for collagen (8.933×10^{-3}), D_s is the measured sample concentration of hydroxyapatite in mg/cm^3, and D_{HA} is the reference density of pure hydroxyapatite (3.16×10^3 mg/cm^3). Collagen birefringence was empirically determined using known-thickness sections of methylmethacrylate-embedded non-mineralized turkey tendon and retardance values from the Rotopol™ system. Reference values for hydroxyapatite are drawn from the CRC Handbook of Chemistry and Physics (Weast & Astle, 1982). The values used here are proportional to those determined by Dallemagne and Melon (1946) for fresh cow bone. Modeling expected birefringence in this way provides a lower bound—departures from the assumption of alignment between bone mineral crystallites and collagen would have the effect of increasing

birefringence and skewing interpreted values of out-of-plane orientation θ toward more longitudinal orientations.

Although specimens were generally aligned with dorsal cortex toward the top of the slide during processing, φ is defined with respect to an arbitrary cross-section orientation during imaging, and does not necessarily have biomechanical significance unless the orientations of all the specimens can be assumed to be 'homologous' or mechanically equivalent in some sense. Even if all specimens are perfectly aligned, most of the biomechanical significance of in-plane CFO in mid-diaphyseal transverse section is related to torsion around a central axis, not to an arbitrary external frame of reference. To preserve the biomechanical significance of in-plane orientation, we adjusted the φ of each pixel to reflect orientation relative to the geometric centroid of the cross section:

$$\varphi_{\text{corr}} = \varphi - \tan^{-1}\left(\frac{v_c}{u_c}\right) + \frac{\pi}{2}$$

where u_c and v_c are the centered values for pixel position coordinates $[u, v]$. This transformation is available as function *centroidCorr()* in *microTransit*. The resulting φ_{corr} values are roughly analogous to φ taken from a cortex that has been "unwrapped" from the centroid into a horizontal sheet. Taken together, the variables θ and φ_{corr} for each pixel provide an additional dimension of CFO when compared conventional circularly polarized light microscopy (CPL).

2.1.5 | Statistical analysis

Angular central Gaussian distribution of orientation

Statistical treatments of orientation data differ in several important respects from those of typical continuous variables. Although in-plane φ_{corr} and out-of-plane θ are recorded by separate variables, their distributions cannot be accurately modeled (or tested) separately. One of the most tractable statistical models of the distribution of axial orientations is the angular central Gaussian (ACG) distribution, which is defined by a transformation matrix $\mathbf{\Lambda}$ such that any sample of three-dimensional orientations $\boldsymbol{X}$ can be transformed to a uniform distribution on a sphere $\boldsymbol{X}_0$ as:

$$\boldsymbol{X}_0 = \frac{\mathbf{\Lambda}^{-\frac{1}{2}}\boldsymbol{X}}{\left(\boldsymbol{X}'\mathbf{\Lambda}^{-1}\boldsymbol{X}\right)^{\frac{1}{2}}}$$

This transformation is roughly analogous to distorting the original measurement space until the collection of $[\theta, \varphi_{corr}]$ orientation vectors in the sample radiates evenly in all directions. The *angGaussSumm()* function in *microTransit* uses Tyler's (Tyler, 1987) maximum likelihood algorithm to estimate $\mathbf{\Lambda}$. Eigenanalysis of the transformation matrix $\mathbf{\Lambda}$ yields a measure of how anisotropic the data are around principal orientation axes (eigenvalues of $\mathbf{\Lambda}$, Figure 3b,c), and also returns the directions of the principal orientation axes (eigenvectors of $\mathbf{\Lambda}$, Figure 3d,e) (Tyler, 1987). Because each pixel of qPLM data in this analysis records a single $[\theta, \varphi_{corr}]$ estimated slow-axis orientation, the orientation characteristics of a given region of bone (e.g., CFO anisotropy, trends in orientation) can be described by the ACG parameters of the pixel set.

Cluster-based regions of interest

Defining regularly spaced regions of interest (ROIs) in Cartesian or polar coordinates is a common means of selecting subsamples of cortical bone for statistical analysis. Although straightforward in concept, this approach carries several assumptions: (a) the orientation of the ROI grid can be matched between specimens, (b) the sampling regions can be considered homologous across specimens, and (c) the distributions of the measured variables are not spatially dependent. Even when these assumptions are met, the accurate placement of ROI grids can be time-consuming.

As an alternative, we use an automated spatially constrained clustering method (Legendre & Legendre, 2012) to define contiguous regions of pixels with similar ACG parameters over 20 × 20 pixel block subsamples across the entire section (Figure 3f). This approach is built into the *qPLMClust()* function in *microTransit*. For this analysis, adjacent subsamples were clustered by similarity in first and second axis $\mathbf{\Lambda}$ eigenvalues (Figure 3b,c) and the z (out-of-plane) component of first and second axis eigenvectors (Figure 3d,e). In mid-diaphyseal cross-sections, these measures are analogous to degree of CFO anisotropy and longitudinal orientation, respectively.

After a hierarchical clustering tree is established for a given image, the tree node(s) that encompass the tissue of interest can be selected for analysis (Figure 3f–h). The *pullCluster()* function in *microTransit* provides an interactive interface for selecting contiguous areas of tissue that cluster together based on ACG parameters. This approach provides a straightforward means to define complex regions of interest, while simultaneously excluding imaging artifacts and local variability outside the biological scope of a given analysis (e.g., secondary osteons in a study of primary bone tissue). The *microTransit* package also provides functions for conventional interactive approaches to ROI selection (drawing a user-defined box or selecting a set number of pixels around a user-defined point).

After cluster-based selection of distinct cortical regions in a section, percentage area for distinct tissue

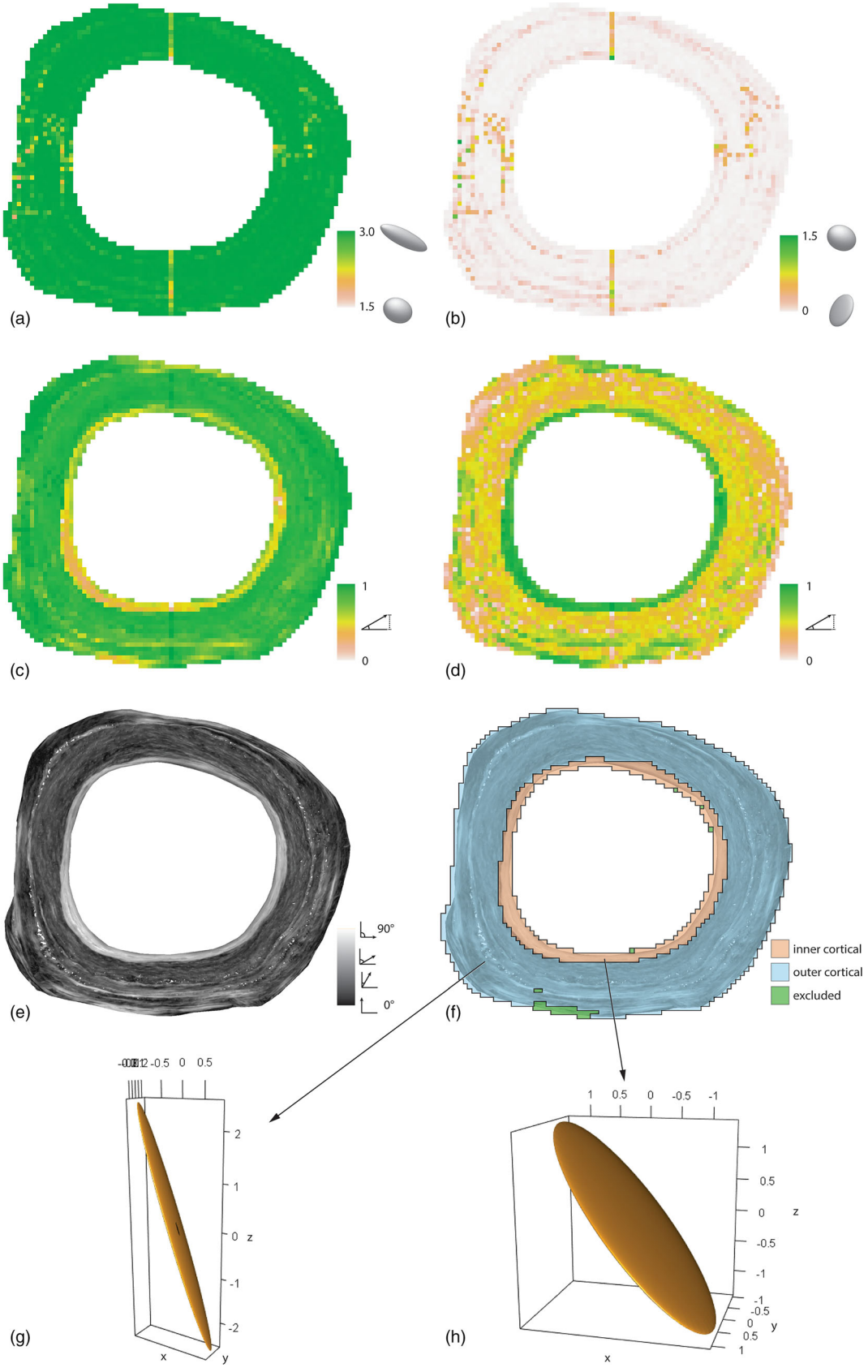

FIGURE 3 Legend on next page.

compartments in each bone were calculated by counting the number of pixels from each selection as a percentage of the total bone pixels from each section's binary mask.

Analysis of age-, bone-, and taxon-related signal

Statistical comparisons of CFO distribution were accomplished using the R package *vegan* (Oksanen et al., 2018). Age class, and the potential confounding variables of taxon, sex, and element (humerus vs. radius vs. metacarpal II), were coded into a design matrix using Helmert contrasts. Variation partitioning analysis (Legendre & Legendre, 2012) was used to assess the joint explanatory power of all categorical variables on CFO distribution, with separate analyses for inner and outer cortical bone compartments. Redundancy analysis (RDA) and an ANOVA-like permutation test which provides an F# statistic comparable to the F statistic of ANOVA (Legendre & Legendre, 2012) were then used to assess the statistical significance of variance partitions in specific models, including (a) a full model with all terms as predictors of CFO distribution, and (b) a model of age as a predictor of CFO distribution, with taxon, sex, and element accounted for as covariates. A similar set of analyses were run for *Eptesicus* by itself, with data from the third metacarpal included. Models for the analysis of *Eptesicus* data included (a) a full model with all terms, (b) a model of age with sex and proximodistal element position as covariates, and (c) a model of proximodistal element position with age and sex as covariates. Each model was tested under 10,000 permutations of the data. Holm correction (Holm, 1979) was used to adjust the significance threshold for multiple non-independent tests.

While the technical aspects of RDA can be complex, the intent of each analysis can be captured as a series of simple questions. Variation partitioning addresses the question: how much of the variation in collagen fiber orientation can be attributed to the effects associated with age, skeletal element, or sex? RDA is a follow-up analysis—the full model addresses the question: can any of the age-, element, or sex-related effects explain a significant proportion of variation in collagen fiber orientation? Conditional models (written as "main effect|covariates") address the question: after other effects are accounted for, can this specific effect (age or proximo-distal gradient) explain a significant proportion of variation in collagen fiber orientation?

3 | RESULTS

3.1 | Zones of cortical bone defined by consistent CFO differences in both taxa

Cluster analysis of cortical bone for both taxa generally returns a single well-supported cluster of more longitudinally oriented bone on the outer region of the cortex continuous with the periosteal surface. An additional 1–4 clusters containing more helically oriented bone lie directly around the endosteal surface (Figure 3f). We will refer to these structurally distinct regions of bone as outer cortical bone and inner cortical bone, respectively. Outer cortical bone tends to show more uniform orientation (greater whole-compartment anisotropy) and more longitudinal orientation than inner cortical bone.

Separate inner cortical bone clusters are absent in all but one of the young C57BL/6 mice and tended to occupy smaller proportions of the overall cortex in elderly vs. middle-aged mice (Figure 4d). Throughout the lifespan of bats, mean values of the percentage of total cortical bone in this inner ring were 6–14 times larger than those of mice (Table 2b, Figure 4c,d). Among bats, only the humerus showed a stepwise decline in the relative size of the inner cortex with age. Elderly bats displayed more inner cortical bone in the radius compared to young and middle-aged bats. In third metacarpals, the size of the inner cortical region was greatest in young bats.

3.2 | Consistent differences between *Eptesicus* and C57BL/6 mice

There are no significant effects of age that are consistent across both taxa. Aside from the presence of recognizable

FIGURE 3 Statistical treatment of qPLM data, illustrated with the Eptesicus radius section from Figure 2. Each cross-section image stack is broken into 20 × 20 pixel subsamples, and the orientation data within each subsample is modeled as an Angular Central Gaussian (ACG) distribution. Four descriptors from this distribution model were used to spatially cluster subsamples: (a) the amplitude of the first eigenvalue of the distribution, analogous to the degree of anisotropy within the subsample; (b) the amplitude of the second eigenvalue, describing a range from single-axis anisotropic to flattened "girdle" distributions; (c) the z component of the first axis eigenvectors, indicating longitudinal anisotropy; and (d) the z component of the second axis eigenvectors, indicating the degree of variability in out-of-plane orientation. Out-of-plane orientation is shown in (e) and (f), with the resulting clusters shown superimposed in (f). Note the area of extrinsic fibers for a muscle attachment that do not cluster with the surrounding cortical bone, shown as 'excluded' in (f). Ellipsoids showing the length and orientation of major ACG axes for the entire ROI are shown for the outer cortical (g) and inner cortical (h) regions. The vertical lines seen in (a) and (b) are artifacts of adjusting φ to φ_{corr}.

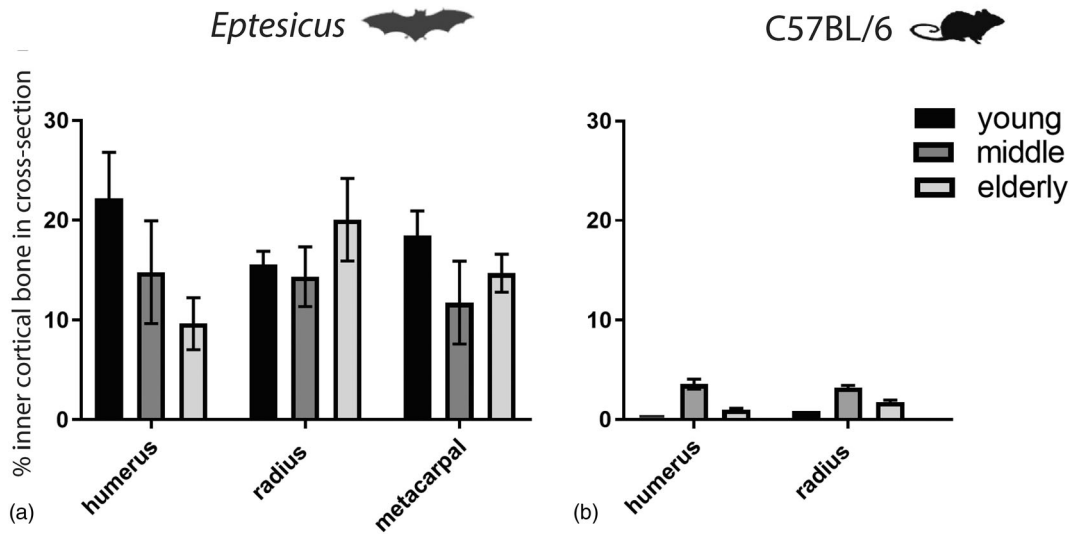

FIGURE 4 Inner cortical bone area over the lifespan of Eptesicus and C57BL/6 mice. Across their lifespan, bats display a greater proportion of inner cortical bone (a) compared to mice (b). Black columns indicate the young age group, dark gray columns indicate the middle-aged group, and the light gray columns indicate the elderly age class.

inner and outer cortical bone regions, both CFO distribution and age-related effects show idiosyncratic taxon-specific patterns. Outer cortical bone tends to be more longitudinal across all elements in *Eptesicus* compared to C57BL/6 mice (Figure 5b). In contrast, inner cortical bone in *Eptesicus* shows a more oblique or helical orientation when compared to C57BL/6 mice (Figure 5a).

3.3 | Consistent characteristics of bone tissue in *Eptesicus*

Across all age groups of *Eptesicus*, both outer and inner cortical bone regions show evidence of a proximodistal gradient in CFO (Figure 6b,d). The effect is more pronounced in outer cortical bone (56% CFO variance explained) than inner cortical bone (12% CFO variance explained). In both cases, more distal elements show more longitudinal CFO and greater overall anisotropy (greater ACG 1st axis eigenvalues, smaller ACG 2nd axis eigenvalues) across the region. Longitudinal orientation has greater influence in this relationship than anisotropy (greater magnitude of loading in RDA).

3.4 | Age-related characteristics of bone tissue in *Eptesicus*

CFO in outer cortical bone shows a small but significant age effect (6% CFO variance explained; Figure 6d). The general trend is an increase in anisotropy and an increase in longitudinal orientation with age. This effect can be seen most clearly in comparisons of θ in the radius among young vs. (middle + elderly) bats, and in the third metacarpal in (young + middle) vs. elderly bats (Figure 5b). In contrast with the proximodistal gradient above, anisotropy varies more consistently with age than longitudinal orientation.

Although it does not contribute to a significant difference in VARPART analysis, there is a noticeable transverse-to-helical trend with age in the inner cortical bone of the radius (Figure 5a).

3.5 | Age-related characteristics of bone tissue in C57BL/6 mice

Inner cortical bone was absent from all but one of the young mice—this single individual showed inner cortical bone that was generally helically aligned ($\theta \approx 45^\circ$) in both humerus and radius, whereas inner cortical bone from older individuals showed a broader range of orientations, with medians of $\theta \approx 60^\circ$ and 55° in humerus and radius, respectively (Figure 5a).

3.6 | Sensitivity of CFO data to collinearity with bone mineral density

Because we apply a scaling for out-of-plane orientation based on expected birefringence from bone mineral density before analysis, one possible interpretation of differences in reported CFO is that they are derived from bone mineral density differences rather than differences in the

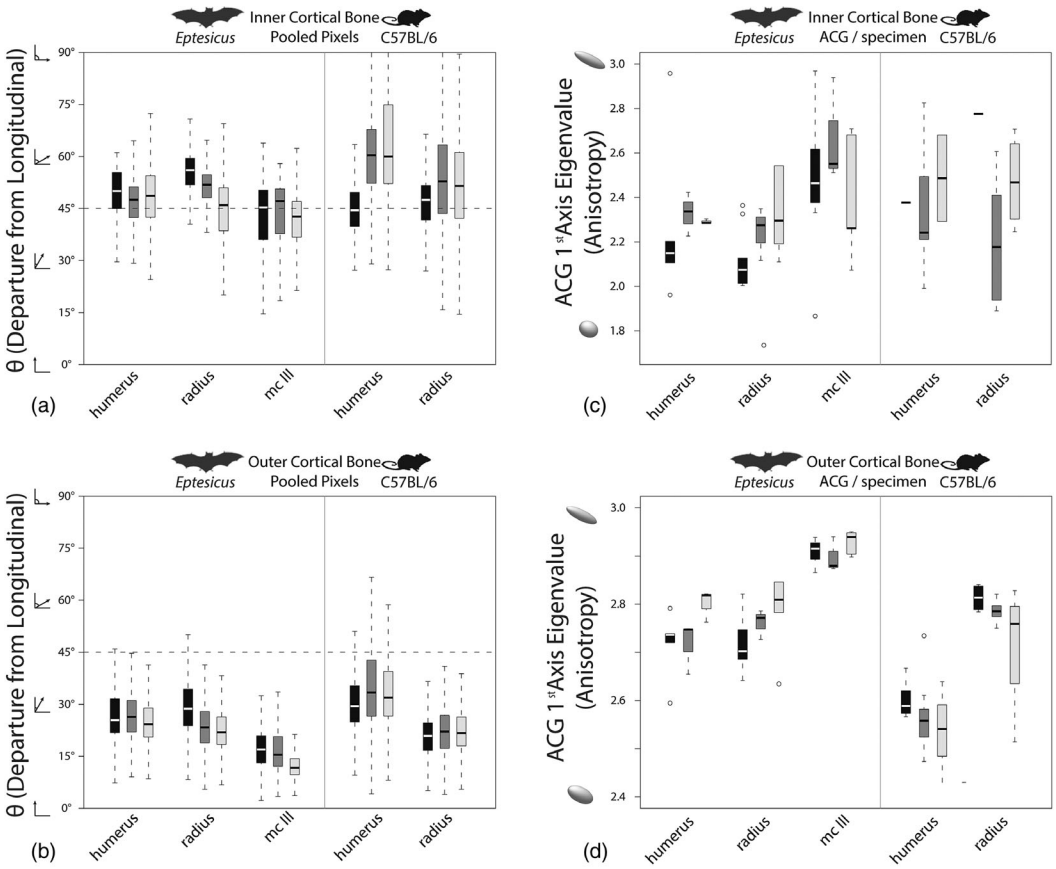

FIGURE 5 Box-and-whisker plot comparisons of out-of-plane collagen fiber orientation θ and anisotropy across samples of young (black), middle-aged (dark gray), and elderly (light gray) bats and mice. Thick white and black lines across boxplots represent the median value, hinges and whiskers represent quartile range. (a) Inner cortical bone θ, pooled from all samples of a given age class and element. Note the trend for Eptesicus inner cortical bone to align more closely with a helical orientation (45°), while inner cortical bone in mice is generally more transversely-oriented. (b) Outer cortical bone. θ, pooled from all samples of a given age class and element. (c) Inner cortical bone anisotropy. (d) Outer cortical bone anisotropy. Note the difference in scale (outer cortical bone is generally more anisotropic that inner cortical bone) as well as the proximodistal gradient of increasing anisotropy in Eptesicus. A similar pattern of increasing anisotropy in distal elements is visible between humerus and radius in mice as well.

underlying fiber orientations themselves. To test for this possibility, we ran a correlation test between our age- and element-class estimates of bone birefringence on one hand and the mean out-of-plane component of CFO for each group on the other. The resulting relationship is not significant ($R^2 = 0.025$, $p = 0.31$), suggesting that our use of estimated birefringence as a scaling factor is not a significant contributor to the shape of our resulting CFO data.

4 | DISCUSSION

Results of our CFO analyses are in agreement with other studies of bats (Lee & Simons, 2015) and laboratory mice (Birkhold et al., 2016; van Tol et al., 2020), that long bones show distinct inner and outer cortical regions. Collagen fibers within the inner cortical region are relatively more helically oriented than the more longitudinally oriented fibers of the outer region in both taxa. Compared to C67BL/6 mice, *Eptesicus* showed a greater concentration of helically oriented fibers within the inner cortical region throughout all age classes, and bone within this region had more oblique or helically oriented fibers compared to those of the mouse. Within the radius of *Eptesicus*, the inner cortical region showed a transition from more transverse to more helically oriented fibers with age. In all measured bats, the outer cortical region trended toward increased anisotropy and longitudinally oriented fibers with age.

In contrast to prior work on bats (Lee & Simons, 2015), we did not isolate a periosteal region of bone tissue as distinct from the outer cortex. There are two differences between our study and that of Lee and

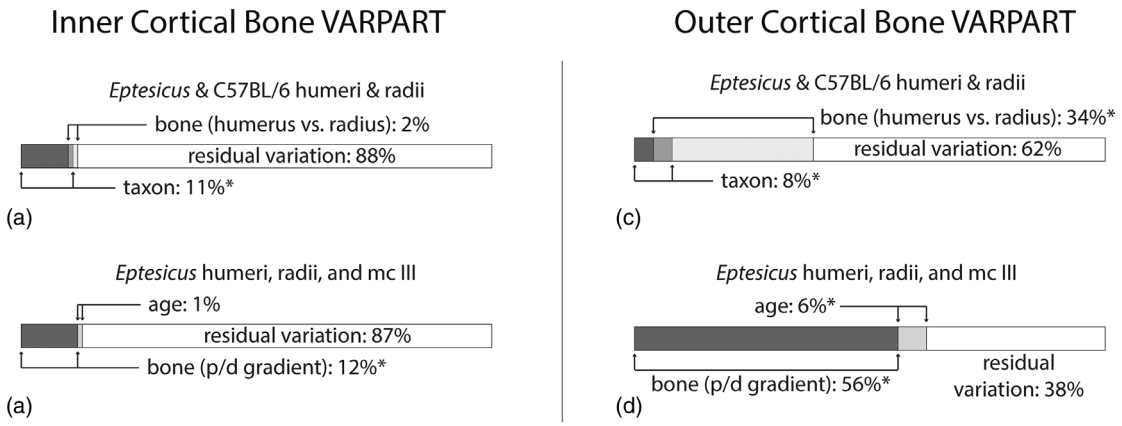

FIGURE 6 (a–d) Results of variation partitioning in RDA analyses, see Tables 3–6. The components shown here are direct readouts of adjusted R^2 values, so each partition of variation also reflects the effect size of a relationship between CFO and the specified independent variable. (a) Variation in inner cortical collagen fiber orientation across both taxa in the humerus and radius. Only taxon explains a significant portion of variation in this sample. Age and sex did not explain measurable portions of variation in the samples and are not shown. (b) Variation in inner cortical collagen fiber orientation in *Eptesicus*. Proximodistal gradient explains a significant portion of variation. Sex does not explain a measurable portion of variation. (c) Variation in outer cortical collagen fiber orientation in both taxa. Bone and taxon both explain significant portions of variation in collagen fiber orientation. Age and sex do not explain measurable portions of variation. (d) Variation in outer cortical collagen fiber orientation in *Eptesicus*. Age and proximodistal gradient both explain significant portions of variation in collagen fiber orientation. Sex does not explain a measurable portion of variation.

Simons (2015) that contribute to this departure. The first is difference in sampling—where prior work focuses on the humerus across several taxa, our work examines humerus, radius, and metacarpals within a single chiropteran taxon. The second difference is that we base our regions on a clustering analysis that uses four collagen fiber orientation parameters across 10 μm × 10 μm subsamples, as compared to visual examination of CPL results. Although there are differences in structure in the periosteal regions of many bat humeri that are apparent to a human observer using CPL, the clustering algorithm typically keyed in on local departures from ACG parameters within the body of the outer cortex before it started isolating anything that could be interpreted as a periosteal region. This is partly due to the fact that when a distinct periosteal organization is present in our samples, it consists of a very thin band that is most likely diluted with other cortical pixels. This is also a reflection of the fact that a distinct periosteal region that would be apparent in CPL is absent in many of our samples. The difference between our study and that of Lee and Simons (2015) suggests that while a distinct periosteal organization is apparent in many taxa, its expression is variable in bats, compared to the relatively invariant presence of an inner cortical bone compartment.

In an osteological study of the Mexican free-tailed bat (*Tadarida brasiliensis*), bones of the wing were shown to decrease in mineral density along a proximo-distal gradient with the most proximal elements being the densest and some distal phalanges lacking bone altogether as they consisted of cartilage (Papadimitriou et al., 1996). Density assays of the wing bones (humerus, radius, and metacarpal) of *Eptesicus* and the bones (humerus and radius) of C57BL/6 mice show a similar proximodistal gradient in bone mineral density (Table 2), although no phalanges were sampled. Results suggest that among bats and mice, the presence of a proximodistal gradient is directly correlated with the material properties of wing bones. Collagen orientations, cross-sectional area, and overall length of the bone may also play a role in determining bone performance.

Unlike the limbs of terrestrial mammals, the wing bones of bats display a unique proximodistal gradient also in performance of their individual bones. Landmark studies showed that during flight, the humerus and radius undergo torsional loading (Swartz et al., 1992), while the metacarpals and phalanges undergo significant bending (Swartz et al., 2007; Swartz & Middleton, 2008). A known influence of bone stiffness or strength in bending or torsional loading is the polar moment of inertia, a measure of the distance of bone about the center of a given cross-section of bone. In the case of *Eptesicus* shown here, as well as a published study of *Myotis* (Kwiecinski et al., 1987), the presence of and even accrual of bone about the inner cortical surface of the bone surrounding the medullary cavity is unlikely to influence bone's polar moment of inertia (Bennett & Forwood, 2010; Currey et al., 2017). The relatively large

inner cortical layer of helically oriented bone in the wing bones of *Eptesicus* is unlikely to influence the bending or torsional stiffness or strength of the elements included in this study. While the inner cortical region is unlikely to influence whole-bone performance, it may instead act on a smaller scale to influence mechano-responsiveness of tissue.

With age, the inner cortical surfaces of mammalian limb bones erode and ultimately osteocytes embedded within the bone matrix decline in mechano-responsiveness with age. These osteocytes and their dendritic processes are embedded within a vast network of lacunae and canaliculi that allow for the cells to sense shear-induced fluid movement within the bone and therefore respond to loading. Osteocytes along the inner cortical, or endosteal, region of bone are known to be more mechano-responsive relative to the outer cortical, or periosteal, compartments of osteocytes, as shown in studies of laboratory mice (Birkhold et al., 2016; van Tol et al., 2020). Because the size of the inner cortical compartment of helically oriented fibers of collagens are larger in bats, it could be that bats retain a relatively larger network of mechano-responsive osteocytes throughout their lifespan. This large network within the wing bones of bats may act as a mineral reservoir that can be modified without weakening the bones and their structurally derived performance. However, no mechanistic testing of the osteocytes taken from either the inner cortical or periosteal compartments have yet been undertaken to test for regional differences in cell mechanosensitivity.

Cortical bone of mammals <5 kg often lacks secondary osteons entirely (Felder et al., 2017). A likely cause is negative allometry of secondary osteon size with respect to cortex size ("volume effect" of Skedros, 2012; see also Currey & Shahar, 2013; Felder et al., 2017; Lad, 2023), which effectively places a lower limit on the thickness of mechanically loaded cortex that can be remodeled by secondary osteons without risking failure of the cortex. We observed cross-cutting relationships among the lamellae of the inner cortical region in several of our *Eptesicus* sections, suggesting that inner cortical bone on the endosteal surface had undergone resorption followed by redeposition of new inner cortical bone in a process of endosteal remodeling (Figure S1). The range of observed thickness of the inner cortical region in *Eptesicus* (<50 μm) is consistent with the mean thickness of secondary osteon infilling in mammals <5 kg (Felder et al., 2017). The cortical regions in most bats are thin enough that the diameter of a newly developing secondary osteon would severely compromise the structure of the cortex (Currey & Shahar, 2013; Felder et al., 2017). A process of inner cortical resorption and redeposition would allow turnover of mechanically responsive bone tissue without compromising the structural properties of the cortex (Currey et al., 2017).

5 | CONCLUSIONS AND FUTURE WORK

This study lays a methodological foundation for future quantitative research into the collagen orientation of mammals via elaborations on standard methods of CFO (see Supplement S1 for further discussion of qPLM as implemented here). Although this study focused on the age-related changes in bone microanatomy in one species of bat compared to a unique strain of laboratory mouse, it remains untested if the bones of bats as a whole differ from those of terrestrial mammals in a similar size range. Bats make an ideal case-study as taxa display a variety of body sizes and locomotor niches (e.g., quadrupedal, different aerial agilities). Study of variation within the wing bones of Chiroptera relative to that seen in small terrestrial mammals may pinpoint how bone tissues of wings differ from those of limbs utilized during terrestrial locomotion. Any contrasts seen in this comparison could also shed light on variation in bone structure among taxa where small cortical size prevents Haversian remodeling, and limits tissue response to modeling and remodeling on the surfaces of the cortex (Felder et al., 2017; Lad, 2023; Skedros, 2012).

This study focuses on testing for age- and element-related patterns CFO. Other data not included in this analysis, such as polar and second moments of area and bone length, would be critical for assessing the potential role of CFO variability in contributing to material properties. If the loading histories of skeletal elements are driving consistent patterns of CFO, these additional data would be necessary as covariates to tease apart the pattern across differences in skeletal element size and shape.

Future comparative in vitro studies may elucidate the molecular mechanisms driving formation of both the inner cortical and periosteal tissues in bat wing bones. Exploration of bone cell signaling and extracellular matrix secretions could offer insight into differential patterning and potential mechanosensitivity of inner outer cortical regions. Ongoing work could isolate and differentiate osteoprogenitor cells from both compartments from known-aged *Eptesicus* following a published protocol (Ball et al., 2016). By exposing cultured cells to loads and quantifying resultant mRNA expression levels and matrix secretions, these data could provide direct evidence of the mechano-responsiveness of bone cells and correlate these findings with the resultant extracellular matrix phenotype. Parallel experiments of cells harvested

from age-matched C57BL/6 mice could offer a more thorough understanding of how these cells differ between terrestrial and volant taxa, as well as highlight differential rates of bone cell senescence between both groups.

AUTHOR CONTRIBUTIONS

Tobin Lee Hieronymus: Conceptualization; investigation; writing – review and editing; methodology; software; formal analysis; data curation; visualization; validation; writing – original draft. **David A. Waugh:** Methodology; investigation; visualization; data curation; writing – review and editing; conceptualization. **Hope C. Ball:** Investigation; data curation. **Christopher J. Vinyard:** Funding acquisition; methodology; formal analysis; writing – review and editing. **Alex Galazyuk:** Resources; conceptualization. **Lisa Noelle Cooper:** Writing – original draft; conceptualization; data curation; supervision; funding acquisition; resources; project administration; writing – review and editing; investigation; validation; visualization.

ACKNOWLEDGMENTS

The authors thank members of NEOMED's Musculoskeletal Research Focus Area for helpful comments on this manuscript, and Dr. Mark T. Clementz for discussions. Andrew Skrinyer is thanked for image analysis. Drs. Jeff Wenstrup and Ellen Covey are thanked for access to animals. Comments from two anonymous reviewers greatly improved the qulaity of the manuscript. Funding for this project came from the U. S. National Science Foundation, Directorate of Engineering. (NSF-CMMI 1537745 to L.N.C. and C.V.).

CONFLICT OF INTEREST STATEMENT

The authors have no conflicts of interest to disclose.

DATA AVAILABILITY STATEMENT

Data used in this study will be made available on DataDryad.

ORCID

Tobin Lee Hieronymus https://orcid.org/0000-0002-0483-5350

REFERENCES

Aido, M., Kerschnitzki, M., Hoerth, R., Checa, S., Spevak, L., Boskey, A. L., Fratzl, P., Duda, G. N., Wagermaier, W., & Willie, B. M. (2015). Effect of *in vivo* loading on bone composition varies with animal age. *Experimental Gerontology*, *63*, 48–58.

Andronowski, J. M., Cole, M. E., Hieronymus, T. L., Davis, R. A., Usher, L. R., & Cooper, L. N. (2022). Intraskeletal consistency in patterns of vascularity within bat limb bones. *Anatomical Record (Hoboken)*, *305*, 462–476.

Ascenzi, A., & Bonucci, E. (1961). A quantitative investigation of the birefringence of the osteon. *Acta Anatomica*, *44*(3), 236–262.

Ascenzi, A., Bonucci, E., Generali, P., Ripamonti, A., & Roveri, N. (1979). Orientation of apatite in single osteon samples as studied by pole figures. *Calcified Tissue International*, *29*, 101–105.

Austad, S. N. (2010). Methusaleh's zoo: How nature provides us with clues for extending human health span. *Journal of Comparative Pathology*, *142*(Suppl 1), S10–S21.

Austad, S. N., & Fischer, K. E. (1991). Mammalian aging, metabolism, and ecology: Evidence from the bats and marsupials. *Journal of Gerontology*, *46*, B47–B53.

Ball, H. C., Levari-Shariati, S., Cooper, L. N., & Aliani, M. (2018). Comparative metabolomics of aging in a long-lived bat: Insights into the physiology of extreme longevity. *PLoS One*, *13*, e0196154.

Ball, H. C., Moussa, F. M., Mbimba, T., Orman, R., Safadi, F. F., & Cooper, L. N. (2016). Methods and insights from the characterization of osteoprogenitor cells of bats (Mammalia: Chiroptera). *Stem Cell Research*, *17*, 54–61.

Beamer, W. G., Donahue, L. R., Rosen, C. J., & Baylink, D. J. (1996). Genetic variability in adult bone density among inbred strains of mice. *Bone*, *18*, 397–403.

Bennett, M. B., & Forwood, M. R. (2010). Histomorphometric changes in the wing bones of the fruit bat, Pteropus poliocephalus, (Megachiroptera: Pteropidae) in relation to increased bone strain. *Australian Zoologist*, *35*, 341–348.

Birkhold, A. I., Razi, H., Duda, G. N., Weinkamer, R., Checa, S., & Willie, B. M. (2016). The periosteal bone surface is less mechano-responsive than the endocortical. *Scientific Reports*, *6*, 23480.

Bonucci, E. (2007). *Biological calcification: Normal and pathological processes in the early stages*. Springer Science & Business Media.

Boyde, A., Bianco, P., Portigliatti Barbos, M., & Ascenzi, A. (1984). Collagen orientation in compact bone: I. A new method for the determination of the proportion of collagen parallel to the plane of compact bone sections. *Metabolic Bone Disease and Related Research*, *5*, 299–307.

Boyde, A., & Riggs, C. M. (1990). The quantitative study of the orientation of collagen in compact bone slices. *Bone*, *11*, 35–39.

Brodt, M. D., Ellis, C. B., & Silva, M. J. (1999). Growing C57Bl/6 mice increase whole bone mechanical properties by increasing geometric and material properties. *Journal of Bone and Mineral Research*, *14*, 2159–2166.

Bromage, T. G. (1992). Microstructural organization and biomechanics of the macaque circumorbital region. In P. Smith & E. Tchernov (Eds.), *Structure, function and evolution of teeth* (pp. 257–272). London Freund Publishing House.

Bromage, T. G., Goldman, H. M., McFarlin, S. C., Warshaw, J., Boyde, A., & Riggs, C. M. (2003). Circularly polarized light standards for investigations of collagen fiber orientation in bone. *The Anatomical Record Part B: The New Anatomist: An Official Publication of the American Association of Anatomists*, *274*, 157–168.

Brunet-Rossinni, A. K., & Austad, S. N. (2004). Ageing studies on bats: A review. *Biogerontology*, *5*, 211–222.

Cooper, L. N., Cretekos, C. J., & Sears, K. E. (2012). The evolution and development of mammalian flight. *WIRES (Wiley Interdisciplinary Reviews: Developmental Biology)*, *1*, 773–779.

Cooper, L. N., & Sears, K. E. (2013). How to grow a bat wing. In R. A. Adams & S. C. Pedersen (Eds.), *Bat evolution, ecology, and conservation* (pp. 3–20). Spring Science + Business Media.

Cooper, L. N., Sears, K. E., Armfield, B. A., Kala, B., Hubler, M., & Thewissen, J. G. M. (2018). Review and experimental evaluation of the embryonic development and evolutionary history of flipper development and hyperphalangy in dolphins (Cetacea: Mammalia). *Genesis*, *56*, e23076.

Currey, J. D., Dean, M. N., & Shahar, R. (2017). Revisiting the links between bone remodelling and osteocytes: Insights from across phyla. *Biological Reviews*, *92*, 1702–1719.

Currey, J. D., & Shahar, R. (2013). Cavities in the compact bone in tetrapods and fish and their effect on mechanical properties. *Journal of Structural Biology*, *183*(2), 107–122.

Dallemagne, M. J., & Melon, J. (1946). Nouvelles recherches relatives aux propriétés optiques de l'os: La biréfringence de l'os minéralisé; Relations entre les fractions organiques et inorganiques de l'os. *Journal of the Washington Academy of Sciences*, *36*(6), 181–195.

De Margerie, E., Sanchez, S., Cubo, J., & Castanet, J. (2005). Torsional resistance as a principal component of the structural design of long bones: Comparative multivariate evidence in birds. *The Anatomical Record Part A: Discoveries in Molecular, Cellular, and Evolutionary Biology*, *282A*, 49–66.

de Medina, P. (2019). Deciphering the metabolic secret of longevity through the analysis of metabolic response to stress on long-lived species. *Medical Hypotheses*, *122*, 62–67.

Dengler-Crish, C. M., Ball, H. C., Lin, L., Novak, K. M., & Cooper, L. N. (2018). Evidence of Wnt/beta-catenin alterations in brain and bone of a tauopathy mouse model of Alzheimer's disease. *Neurobiology of Aging*, *67*, 148–158.

Dengler-Crish, C. M., Smith, M. A., & Wilson, G. N. (2016). Early evidence of low bone density and decreased serotonergic synthesis in the dorsal raphe of a tauopathy model of Alzheimer's disease. *Journal of Alzheimer's Disease*, *55*, 1605–1619.

Doherty, A., & de Magalhaes, J. P. (2016). Has gene duplication impacted the evolution of eutherian longevity? *Aging Cell*, *15*, 978–980.

Felder, A. A., Phillips, C., Cornish, H., Cooke, M., Hutchinson, J. R., & Doube, M. (2017). Secondary osteons scale allometrically in mammalian humerus and femur. *Royal Society Open Science*, *4*(11), 170431.

Ferguson, V. L., Ayers, R. A., Bateman, T. A., & Simske, S. J. (2003). Bone development and age-related bone loss in male C57BL/6J mice. *Bone*, *33*, 387–398.

Flurkey, K., Currer, J. M., & Harrison, D. (2007). The mouse in aging research. In J. G. Fox, M. T. Davisson, C. E. Newcomer, F. W. Quimby, & A. L. Smith (Eds.), *The mouse in biomedical research* (pp. 637–672). American College Laboratory Animal Medicine (Elsevier).

Foote, J. (1916). A contribution to the comparative histology of the femur. *Smithsonian Contributions to Knowledge*, *35*, 1–231.

Glazer, A., Lewis, J., & Kaminsky, W. (1996). An automatic optical imaging system for birefringent media. *Proceedings of the Royal Society of London. Series A: Mathematical, Physical and Engineering Sciences*, *452*, 2751–2765.

Goldman, H. M., Bromage, T. G., Thomas, C. D., & Clement, J. G. (2003). Preferred collagen fiber orientation in the human midshaft femur. *The Anatomical Record. Part A, Discoveries in Molecular, Cellular, and Evolutionary Biology*, *272*, 434–445.

Gomes, N. M., Ryder, O. A., Houck, M. L., Charter, S. J., Walker, W., Forsyth, N. R., Austad, S. N., Venditti, C., Pagel, M., Shay, J. W., & Wright, W. E. (2011). Comparative biology of mammalian telomeres: Hypotheses on ancestral states and the roles of telomeres in longevity determination. *Aging Cell*, *10*, 761–768.

Halloran, B. P., Ferguson, V. L., Simske, S. J., Burghardt, A., Venton, L. L., & Majumdar, S. (2002). Changes in bone structure and mass with advancing age in the male C57BL/6J mouse. *Journal of Bone and Mineral Research*, *17*, 1044–1050.

Hockman, D., Cretekos, C. J., Mason, M. K., Behringer, R. R., Jacobs, D. S., & Illing, N. (2008). A second wave of sonic hedgehog expression during the development of the bat limb. *Proceedings of the National Academy of Sciences*, *105*, 16982–16987.

Holguin, N., Brodt, M. D., Sanchez, M. E., & Silva, M. J. (2014). Aging diminishes lamellar and woven bone formation induced by tibial compression in adult C57BL/6. *Bone*, *65*, 83–91.

Holm, S. (1979). A simple sequentially rejective multiple test procedure. *Scandinavian Journal of Statistics*, 65–70.

Huang, Z., Whelan, C. V., Foley, N. M., Jebb, D., Touzalin, F., Petit, E. J., Puechmaille, S. J., & Teeling, E. C. (2019). Longitudinal comparative transcriptomics reveals unique mechanisms underlying extended healthspan in bats. *Nature Ecology & Evolution*, *3*, 1110–1120.

Jilka, R. L. (2013). The relevance of mouse models for investigating age-related bone loss in humans. *The Journals of Gerontology. Series A, Biological Sciences and Medical Sciences*, *68*, 1209–1217.

Kaminsky, W., Gunn, E., Sours, R., & Kahr, B. (2007). Simultaneous false-colour imaging of birefringence, extinction and transmittance at camera speed. *Journal of Microscopy*, *228*, 153–164.

Kwiecinski, G. G., Krook, L., & Wimsatt, W. A. (1987). Annual skeletal changes in the little brown bat, *Myotis lucifugus lucifugus*, with particular reference to pregnancy and lactation. *The American Journal of Anatomy*, *178*, 410–420.

Lad, S. E. (2023). Absence of secondary osteons in femora of aged rats: Implications of lifespan on haversian remodeling in mammals. *Journal of Morphology*, *284*(7), e21600.

Lee, A. H., & Simons, E. L. R. (2015). Wing bone laminarity is not an adaptation for torsional resistance in bats. *PeerJ*, *3*, e823.

Legendre, P., & Legendre, L. (2012). *Numerical ecology*. Elsevier.

Lidzbarsky, G., Gutman, D., Shekhidem, H. A., Sharvit, L., & Atzmon, G. (2018). Genomic instabilities, cellular senescence, and aging: *In vitro*, *in vivo* and aging-like human syndromes. *Frontiers in Medicine*, *5*, 104.

Lucas, K. N., Johnson, N., Beaulieu, W. T., Cathcart, E., Tirrell, G., Colin, S. P., Gemmell, B. J., Dabiri, J. O., & Costello, J. H. (2014). Bending rules for animal propulsion. *Nature Communications*, *5*, 3293.

Ma, S., & Gladyshev, V. N. (2017). Molecular signatures of longevity: Insights from cross-species comparative studies. *Seminars in Cell & Developmental Biology*, *70*, 190–203.

Mardia, K., & Jupp, P. (2000). *Directional statistics*. John Wiley & Sons.

Munshi-South, J., & Wilkinson, G. S. (2010). Bats and birds: Exceptional longevity despite high metabolic rates. *Ageing Research Reviews*, *9*, 12–19.

Nesse, W. D. (2004). *Introduction to optical mineralogy*. Oxford University Press.

Oksanen, J., Guillaume Blanchet, F., Friendly, M., Kindt, R., Legendre, P., McGlinn, D., Minchin, P. R., O'Hara, R. B., Simpson, G. L., Solymos, P., Stevens, M. H. H., Szoecs, E., & Wagner, H. (2018). *Vegan: Community ecology package. R package version 2.5-2*. https://CRAN.R-project.org/package=vegan

Oldenbourg, R., & Mei, G. (1995). New polarized light microscope with precision universal compensator. *Journal of Microscopy*, *180*, 140–147.

Papadimitriou, H. M., Swartz, S. M., & Kunz, T. H. (1996). Ontogenetic and anatomic variation in mineralization of the wing skeleton of the Mexican free-tailed bat, *Tadarida brasiliensis*. *Journal of Zoology*, *240*, 411–426.

Podlutsky, A. J., Khritankov, A. M., Ovodov, N. D., & Austad, S. N. (2005). A new field record for bat longevity. *The Journals of Gerontology Series A: Biological Sciences and Medical Sciences*, *60*, 1366–1368.

Pratt, I. V., Johnston, J. D., Walker, E., & Cooper, D. M. L. (2018). Interpreting the three-dimensional orientation of vascular canals and cross-sectional geometry of cortical bone in birds and bats. *Journal of Anatomy*, *232*, 931–942.

Pride, H., Yu, Z., Sunchu, B., Mochnick, J., Coles, A., Zhang, Y., Buffenstein, R., Hornsby, P. J., Austad, S. N., & Pérez, V. I. (2015). Long-lived species have improved proteostasis compared to phylogenetically-related shorter-lived species. *Biochemical and Biophysical Research Communications*, *457*, 669–675.

R Core Team. (2018). *R: A language and environment for statistical computing*. R Foundation for Statistical Computing.

Raghavan, M., Sahar, N. D., Kohn, D. H., & Morris, M. D. (2012). Age-specific profiles of tissue-level composition and mechanical properties in murine cortical bone. *Bone*, *50*, 942–953.

Salmon, A. B., Leonard, S., Masamsetti, V., Pierce, A., Podlutsky, A. J., Podlutskaya, N., Richardson, A., Austad, S. N., & Chaudhuri, A. R. (2009). The long lifespan of two bat species is correlated with resistance to protein oxidation and enhanced protein homeostasis. *The FASEB Journal*, *23*, 2317–2326.

Sears, K. E., Behringer, R. R., Rasweiler, J. J., & Niswander, L. A. (2006). Development of bat flight: Morphologic and molecular evolution of bat wing digits. *Proceedings of the National Academy of Sciences*, *103*, 6581–6586.

Sekita, A., Matsugaki, A., Ishimoto, T., & Nakano, T. (2017). Synchronous disruption of anisotropic arrangement of the osteocyte network and collagen/apatite in melanoma bone metastasis. *Journal of Structural Biology*, *197*, 260–270.

Seluanov, A., Gladyshev, V. N., Vijg, J., & Gorbunova, V. (2018). Mechanisms of cancer resistance in long-lived mammals. *Nature Reviews. Cancer*, *18*, 433–441.

Sheng, M. H. C., Baylink, D. J., Beamer, W. G., Donahue, L. R., Rosen, C. J., Lau, K. H. W., & Wergedal, J. E. (1999). Histomorphometric studies show that bone formation and bone mineral apposition rates are greater in C3H/HeJ (high-density) than C57BL/6J (low-density) mice during growth. *Bone*, *25*, 421–429.

Skedros, J. G. (2012). Interpreting load history in limb-bone diaphyses: Important considerations and their biomechanical foundations. In Crowder, C., & Stout, S. (Eds.): *Bone Histology: An Anthropological Perspective*, (pp.153–220). CRC Press.

Skedros, J. G., & Doutré, M. S. (2019). Collagen fiber orientation pattern, osteon morphology and distribution, and presence of laminar histology do not distinguish torsion from bending in bat and pigeon wing bones. *Journal of Anatomy*, *0*, 748–763.

Skedros, J. G., Mendenhall, S. D., Kiser, C. J., & Winet, H. (2009). Interpreting cortical bone adaptation and load history by quantifying osteon morphotypes in circularly polarized light images. *Bone*, *44*(3), 392–403.

Skedros, J. G., Sorenson, S. M., Takano, Y., & Turner, C. H. (2006). Dissociation of mineral and collagen orientations may differentially adapt compact bone for regional loading environments: Results from acoustic velocity measurements in deer calcanei. *Bone*, *39*(1), 143–151.

Skrinyer, A. J., Faure, P. A., Dannemiller, S., Ball, H. C., Delaney, K. H., Orman, R., Stewart, M., & Cooper, L. N. (2017). Care and husbandry flying mammals. *Laboratory Animal Science*, *6*, 24–27.

Spiesz, E. M., Kaminsky, W., & Zysset, P. K. (2011). A quantitative collagen fibers orientation assessment using birefringence measurements: Calibration and application to human osteons. *Journal of Structural Biology*, *176*, 302–306.

Spiesz, E. M., Reisinger, A. G., Kaminsky, W., Roschger, P., Pahr, D. H., & Zysset, P. K. (2013). Computational and experimental methodology for site-matched investigations of the influence of mineral mass fraction and collagen orientation on the axial indentation modulus of lamellar bone. *Journal of the Mechanical Behavior of Biomedical Materials*, *28*, 195–205.

Spiesz, E. M., Thorpe, C. T., Thurner, P. J., & Screen, H. R. C. (2018). Structure and collagen crimp patterns of functionally distinct equine tendons, revealed by quantitative polarised light microscopy (qPLM). *Acta Biomaterialia*, *70*, 281–292.

Srinivasan, S., Agans, S. C., King, K. A., Moy, N. Y., Poliachik, S. L., & Gross, T. S. (2003). Enabling bone formation in the aged skeleton via rest-inserted mechanical loading. *Bone*, *33*, 946–955.

Stokes, A. R. (1963). *The theory of the optical properties of inhomogeneous materials*. E & F.N. Spon, London.

Swartz, S., Iriarte-Diaz, J., Riskin, D., Tian, X., Song, A., & Breuer, K. (2007). Wing structure and the aerodynamic basis of flight in bats. In *45th AIAA aerospace sciences meeting and exhibit*. American Institute of Aeronautics and Astronautics.

Swartz, S. M., Bennett, M. B., & Carrier, D. R. (1992). Wing bone stresses in free flying bats and the evolution of skeletal design for flight. *Nature*, *359*, 726–729.

Swartz, S. M., & Middleton, K. M. (2008). Biomechanics of the bat limb skeleton: Scaling, material properties and mechanics. *Cells, Tissues, Organs*, *187*, 59–84.

Syed, F. A., Iqbal, J., Peng, Y., Sun, L., & Zaidi, M. (2010). Clinical, cellular and molecular phenotypes of aging bone. *Interdisciplinary Topics in Gerontology*, *37*, 175–192.

Takano, Y., Turner, C. H., & Burr, D. B. (1996). Mineral anisotropy in mineralized tissues is similar among species and mineral growth occurs independently of collagen orientation in rats: Results from acoustic velocity measurements. *Journal of Bone and Mineral Research*, *11*(9), 1292–1301.

Tyler, D. E. (1987). Statistical analysis for the angular central gaussian distribution on the sphere. *Biometrika*, *74*, 579–589.

van Tol, A. F., Schemenz, V., Wagermaier, W., Roschger, A., Razi, H., Vitienes, I., Fratzl, P., Willie, B. M., & Weinkamer, R. (2020). The mechanoresponse of bone is closely related to the osteocyte lacunocanalicular network architecture. *Proceedings*

of the National Academy of Sciences of the United States of America, *117*, 32251–32259.

Warshaw, J., Bromage, T. G., Terranova, C. J., & Enlow, D. H. (2017). Collagen fiber orientation in primate long bones. *The Anatomical Record*, *300*, 1189–1207.

Weast, R. C., & Astle, M. J. (1982). *CRC handbook of chemistry and physics (1981–1982)* (B203). CRC Press Inc.

Weatherbee, S., Behringer, R., Rasweiler, J., & Niswander, L. (2006). Interdigital webbing retention in bat wings illustrates genetic changes underlying amniote limb diversification. *Proceedings of the National Academy of Sciences of the United States of America*, *103*, 15103–15107.

Wilkinson, G. S., & Adams, D. M. (2019). Recurrent evolution of extreme longevity in bats. *Biology Letters*, *15*, 20180860.

Wilkinson, G. S., Adams, D. M., Haghani, A., Lu, A. T., Zoller, J., Breeze, C. E., Arnold, B. D., Ball, H. C., Carter, G., Cooper, L. N., Dechmann, D. K., Devanna, P., Fasel, N. J., Galazyuk, A. V., Günther, L., Hurme, E., Jones, G., Knörnschild, M., Lattenkamp, E. Z., … Horvath, S. (2020). Genome methylation predicts age and longevity of bats. *bioRxiv*. https://doi.org/10.1101/2020.09.04.283655

Wilkinson, G. S., Adams, D. M., Haghani, A., Lu, A. T., Zoller, J., Breeze, C. E., Arnold, B. D., Ball, H. C., Carter, G. G., Cooper, L. N., Dechmann, D. K. N., Devanna, P., Fasel, N. J., Galazyuk, A. V., Günther, L., Hurme, E., Jones, G., Knörnschild, M., Lattenkamp, E. Z., … Horvath, S. (2021). DNA methylation predicts age and provides insight into exceptional longevity of bats. *Nature Communications*, *12*(1), 1615.

Wilkinson, G. S., & South, J. M. (2002). Life history, ecology and longevity in bats. *Aging Cell*, *1*, 124–131.

Yang, B., Jan, N.-J., Brazile, B., Voorhees, A., Lathrop, K. L., & Sigal, I. A. (2018). Polarized light microscopy for 3-dimensional mapping of collagen fiber architecture in ocular tissues. *Journal of Biophotonics*, *11*, e201700356.

Yuan, R., Tsaih, S. W., Petkova, S. B., de Evsikova, C. M., Xing, S., Marion, M. A., Bogue, M. A., Mills, K. D., Peters, L. L., Bult, C. J., Rosen, C. J., Sundberg, J. P., Harrison, D. E., Churchill, G. A., & Paigen, B. (2009). Aging in inbred strains of mice: Study design and interim report on median lifespans and circulating IGF1 levels. *Aging Cell*, *8*, 277–287.

SUPPORTING INFORMATION

Additional supporting information can be found online in the Supporting Information section at the end of this article.

How to cite this article: Hieronymus, T. L., Waugh, D. A., Ball, H. C., Vinyard, C. J., Galazyuk, A., & Cooper, L. N. (2023). Comparing age- and bone-related differences in collagen fiber orientation: A case study of bats and laboratory mice using quantitative polarized light microscopy. *The Anatomical Record*, 1–19. https://doi.org/10.1002/ar.25368